Applied Physics B (2023) 129:33
https://doi.org/10.1007/s00340-023-07969-1

Applied Physics B
Lasers and Optics

RESEARCH

Design, construction and characterisation of a diode-pumped, three-element, 1-GHz Kerr-lens-modelocked Ti:sapphire oscillator

Hanna Ostapenko[1] · Toby Mitchell[1] · Pablo Castro-Marin[1] · Derryck T. Reid[1]

Received: 29 November 2022 / Accepted: 8 January 2023 / Published online: 30 January 2023

Abstract
We present a design and construction prescription for a 1-GHz repetition rate Ti:sapphire laser pumped with a single green pump diode and with a resonator comprising as few as three optical elements. In a three-element configuration, the laser produces 111-fs pulses and exhibits self-starting Kerr-lens modelocking at pump powers above 850 mW. At 1.1 W of pump power, the average output of the laser is over 116 mW, and the slope efficiency is measured to be 13%. With the addition of a fourth dispersion-compensating element to optimise the second-order group-delay intracavity dispersion, we have demonstrated a reduction of the pulse durations to 87 fs with an average power of 108 mW.

1 Introduction

Diode pumping of Ti:sapphire lasers has been repeatedly investigated in the past decade since it offers a significant reduction in complexity of the pump laser at the cost of more sophisticated beam formatting [1, 2]. Moreover, high-power laser diode sources at blue and green wavelengths have been in constant development, with high-efficiency Watt-class diodes reported in the last decade constantly evolving in their beam quality but still providing a highly astigmatic output [3, 4]. Effective beam shaping has been key to providing efficient mode matching with the cavity mode, which is essential for designs utilising Kerr-lens modelocking to produce short pulses [5]. Combined with the relatively low powers of the diodes in the blue and green, it is challenging to achieve GHz-level repetition rates from modelocked Ti:sapphire systems, especially while using a single diode. However, such systems show great potential for laser frequency combs since direct modulation of pump diode power allows high-speed control of the carrier envelope offset frequency [6, 7].

Here, we develop and extend our previously published results from a 1-GHz self-starting Ti:sapphire oscillator pumped by a single green diode [8]. We provide an in-depth description of the modelling method used and detail the pumping arrangement and design, whose optimisation is critical to the laser performance. We also expand on the pump diode specifications and the in-cavity dispersion optimisation to highlight the potential for further reduction of the pulse durations compared to our originally reported laser while still maintaining the simplicity of the system.

2 Oscillator design and construction

2.1 ABCD resonator model for optimised Kerr-lens modelocking

The laser, as described in [8], is designed as a three-element oscillator with a plane-Brewster geometry of the Ti:sapphire gain crystal as shown in Fig. 1a with a photograph of the cavity in Fig. 1b. The cavity is designed to collimate the output beam through the same lens used to focus the pump beam into the crystal, and a dichroic beam splitter is used to separate the two beams. The end mirror is mounted on a piezo-transducer (PZT) for the cavity length control.

Extensive modelling of the cavity was used to determine the operating distances for obtaining the best laser performance, the optimal crystal insertion and to determine the requirements for the pump beam focussing. The resonator design is shown in Fig. 2, in which the intracrystal distance is l, the distance from the Brewster face of the crystal to the curved mirror is d_1, and the distance

✉ Hanna Ostapenko
ho14@hw.ac.uk

[1] Scottish Universities Physics Alliance (SUPA), Institute of Photonics and Quantum Sciences, School of Engineering and Physical Sciences, Heriot-Watt University, Edinburgh EH14 4AS, UK

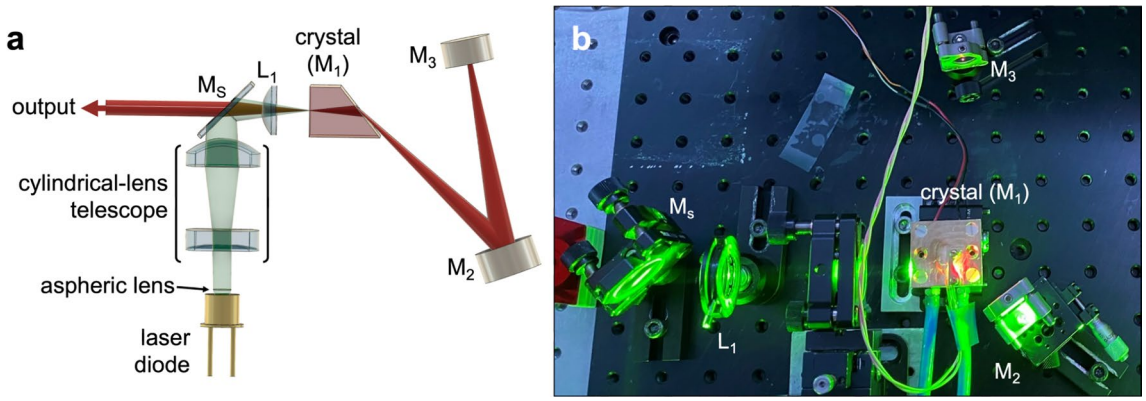

Fig. 1 **a** Oscillator design. M_S—separator mirror; L_1—focussing lens; crystal (M_1)—Ti:sapphire crystal with the 1% OC coating on the plane surface; M_2—curved pump mirror with $R = 50$ mm; M_3—plane HR mirror with GDD = − 550 fs^2 coating on a PZT. **b** Photograph of the laser in operation

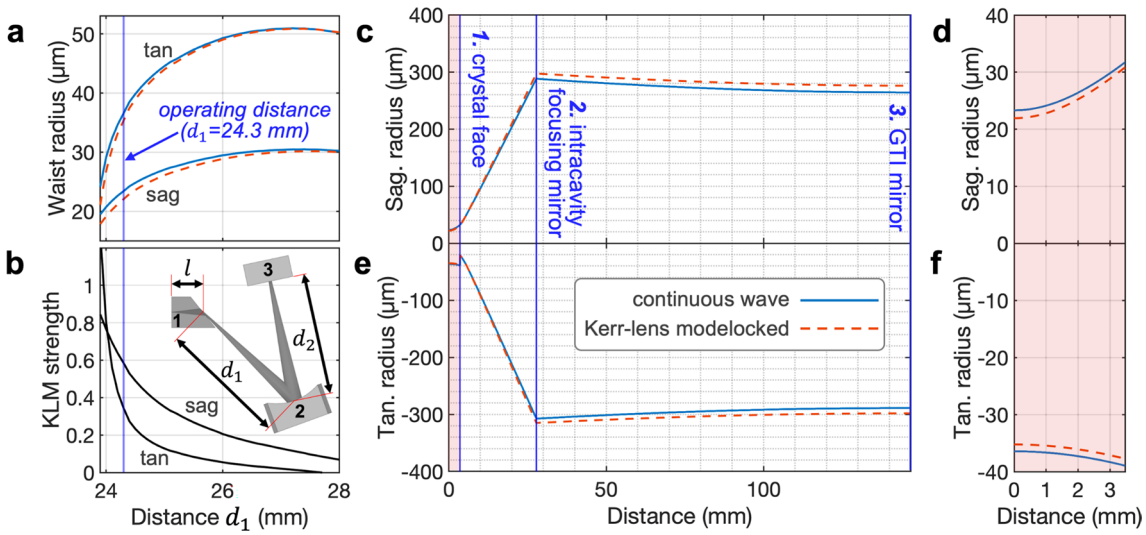

Fig. 2 **a** Tangential and sagittal beam waist radii ($1/e^2$ intensities) on the crystal entrance face for cw (solid blue) and Kerr-lens modelocked (dashed red) operation. **b** Kerr-lens modelocking strength, showing a stronger Kerr effect for shorter crystal-mirror distances for both sagittal (sag) and tangential (tan) rays. Inset: resonator geometry and parameter definitions for the three-element Kerr-lens-modelocked laser. **c** Sagittal beam radius throughout the whole cavity and **d** detail of the beam radius inside the Ti:sapphire crystal. **e** and **f**: corresponding behaviour for tangential rays

from this mirror to the plane end mirror is d_2. The resonator was modelled using the ABCD formalism described in [9] and [10] and for which the relevant ABCD matrices are presented in Table 1. A parabolic duct model was used to represent the Kerr lens [11, 12]. In [11], the astigmatism of the cavity is not included, so we extended the model to include this by incorporating the appropriate focussing behaviours of the curved mirror in the tangential and sagittal planes.

Propagation through the crystal (length l) is a critical element of the model. As detailed in [12], the parabolic duct is represented as an inverted parabola of the form:

$$n = n_o\left(1 - \frac{r^2}{2h^2}\right)$$

where

$$h = \frac{w^2}{2}\sqrt{\frac{n_o \pi a}{2n_2 P}},$$

where w is the $1/e^2$ beam radius, n_o and n_2 are the linear and nonlinear refractive indices of the Ti:sapphire crystal, P is the pulse peak power and a is a correction factor [13] compensating for the differences between the parabolic duct and the Gaussian duct that more accurately represents the

Table 1 ABCD matrices forming the Kerr-lens propagation model

Cavity element	ABCD propagation matrix
Propagation, distance d in a medium of refractive index n	$M_{freespace} = \begin{pmatrix} 1 & d/n \\ 0 & 1 \end{pmatrix}$
Thin lens, focal length f	$M_{lens} = \begin{pmatrix} 1 & 0 \\ -\frac{1}{f} & 1 \end{pmatrix}$
Curved mirror, tangential reflection at angle θ and with focal length f	$M_{Sag} = \begin{pmatrix} 1 & 0 \\ -\frac{1}{f\cos\theta} & 1 \end{pmatrix}$
Curved mirror, sagittal reflection at angle θ and with focal length f	$M_{Tan} = \begin{pmatrix} 1 & 0 \\ -\frac{\cos\theta}{f} & 1 \end{pmatrix}$
Brewster entrance/exit interface	$M_{Brewster} = \begin{pmatrix} \frac{\cos\theta_2}{\cos\theta_1} & 0 \\ 0 & \frac{\cos\theta_1}{\cos\theta_2} \end{pmatrix}$ $\theta_2 = sin^{-1}\left(\frac{n_1 sin\theta_1}{n_2}\right)$
GRIN lens for Kerr nonlinearity [12]	$M_{Kerr} = \begin{pmatrix} 1 - \frac{dz^2}{2h^2} & \frac{dz}{n_o} \\ -\frac{n_o dz}{h^2} & 1 - \frac{dz^2}{2h^2} \end{pmatrix}$

Kerr lens. Since the power in the crystal should never exceed the critical power for self-focussing ($P_{crit} = a\lambda^2/8\pi n_o n_2$), it is convenient to conduct the analysis in terms of P_{crit}, so the model considers the stable intracavity beam solutions for cw operation ($P \ll P_{crit}$) and modelocked operation ($P = 0.1P_{crit}$). Propagation through the crystal is implemented by dividing it into N sections, each of length $dz = l/N$. For each section, the current (k^{th}) value of the beam radius, w_k, allows the local duct parameter, h, to be obtained, which is used to calculate M_{Kerr} and obtain an updated value for the complex beam parameter by applying the propagation law:

$$q_{k+1} = \frac{Aq_k + B}{Cq_k + D},$$

where A, B, C and D are the elements of M_{Kerr}. Correspondingly, an updated value for the beam radius, w_{k+1}, is obtained from the definition of the complex beam parameter:

$$\frac{1}{q_{k+1}} = \frac{1}{R_{k+1}} - \frac{i\lambda}{\pi w_{k+1}^2}$$

where λ is the wavelength in air, since the refractive index of the crystal is already accounted for in M_{Kerr}.

We consider propagation of both sagittal and tangential rays, which are treated identically inside the crystal, but we exit the crystal at its Brewster-angled face by applying $M_{Brewster}$ for tangential rays, while for sagittal rays, no matrix is needed. From the crystal to the curved mirror, we divide the distance d_1 into N steps, each of length dz, and apply $M_{freespace}$ and the propagation law, calculating and recording w, q and z at every position. We apply M_{Sag} or M_{Tan} and the propagation law to find q and w after the mirror for the sagittal and tangential rays, respectively, and then propagate the distance d_2 to the end mirror in the same way as before.

Resonator stability is found by an iterative process implemented in MATLAB® which, for specified values of l, d_1 and d_2, seeks to determine the beam radius of a plane wave at the entrance face of the crystal which yields a plane wave on the end mirror. This condition corresponds to forming beam waists at opposite ends of the resonator, as required for stability. The model is configured as a function which receives an initial guess for the crystal beam waist radius and returns a value proportional to $|1/R|$, where R is the wavefront curvature on the end mirror. The MATLAB® function fminsearch is used to minimise $|1/R|$ and so find a stable solution corresponding to a plane wave on the end mirror.

In Fig. 2, we show some results from this model of stable resonator solutions and their corresponding beam radii. In Fig. 2a, we present the tangential and sagittal beam waist radii on the crystal entrance face for cw and Kerr-lens modelocked operation for different separations of the crystal and curved mirror. The strength of the Kerr-lens effect can be quantified by a parameter representing the change in the beam waist size due to the nonlinearity, normalised to the linear waist evaluated in the limit of low power [14–16], and shows (Fig. 2b) that the strongest Kerr-lens action occurs when the curved mirror is closest to the crystal. From measurement, we estimated the actual operating point of our laser corresponded to a crystal insertion of $l = 3.5$ mm and a distance of $d_1 = 24.3$ mm, indicated in Fig. 2a and b by the vertical blue line. In this condition, the mode area reduces by around 10% when the laser transitions from cw to Kerr-lens-modelocked operation [17]. In Fig. 2c–f, we present the corresponding beam radii in the tangential and sagittal planes for the stable intracavity mode.

The advanced modelling described here allowed a more detailed investigation of the cavity mode change between the cw and modelocked mode of operation. From Fig. 2d and f, the predicted cw cavity mode corresponds to a focal spot of 24 µm × 36 µm, which reduces to 22 µm × 35 µm when the laser modelocks. Moreover, the cavity beam waist is at the plane side of the Ti:sapphire crystal, corresponding to the position for the pump focussing for optimal mode matching.

2.2 Diode-pumping scheme and pump-beam formatting

Single laser diodes, while providing a cheaper and often more compact solution for pumping purposes as opposed to bulky DPSS modules, require appropriate beam conditioning for efficient mode matching due to their highly divergent elliptical output. A single multimode Nichia NDG7D75 diode was chosen for pumping with a typical maximum optical output power up to 1.5 W. Due to its multimode

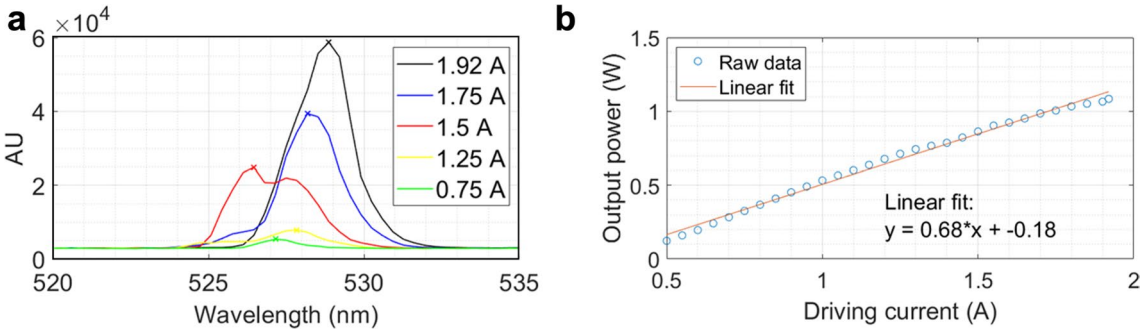

Fig. 3 **a** Diode output spectral changes depending on the driving current, with the spectral peaks highlighted by crosses; **b** measured slope efficiency of the diode along the operating range

nature, the spectral performance of the diode was observed to change depending on the driving current as shown in Fig. 3a. The slope efficiency of the diode was estimated to be 680 mW A^{-1} as shown in Fig. 3b which was within the quoted range. The diode was set to operate at a driving current up to 1.9 A, corresponding to a maximum optical output power of 1.1 W and a central optical wavelength of 529 nm.

The typical beam divergence of the diode was quoted to be up to a full angle of 8.2° along the slow axis (parallel to the pn junction of the diode) and 42° of fast (perpendicular) axis. An aspheric lens of $f = 4.02$ mm was integrated immediately after the diode output to collimate the fast axis, although imperfect collimation meant that the slow axis remained slightly divergent as illustrated in Fig. 4a. The beam conditioning was developed in a step-wise fashion. First, an achromatic doublet lens with $f = 35$ mm was used to focus the beam as shown in Fig. 4b, resulting in a 209 µm × 34 µm elliptical spot where the dimensions are measured to be the full-width at half maximum (FWHM) spot diameter across one axis. Correspondingly, a 6:1 cylindrical lens telescope was constructed to compensate the slow-axis divergence, where a first lens of $f = -50$ mm was used to expand (Fig. 4c and d) and a second lens of $f = +300$ mm was used to collimate the beam along the slow axis (Fig. 4e and f), resulting in a more symmetrical focal spot with dimensions of 11 µm × 7 µm. This beam formatting procedure made it possible to tightly focus both slow and fast axes at a common plane, with fine adjustment being possible by making small changes to the separation between the cylindrical lenses.

To better fit the predicted cavity mode estimated through modelling as highlighted in Fig. 2d and f, a different focussing lens was used with $f = 45$ mm, which was measured to produce a FWHM focal spot of 18.5 µm × 20.1 µm, corresponding to $1/e^2$ radii of 15.7 µm × 17.1 µm. This pump-spot size is smaller than the cavity mode focal size at Kerr-lens modelocked operation predicted through the modelling of 22 µm × 35 µm but was found to provide the best laser operation for the lenses available ($f = 35$ mm and $f = 80$ mm). Experimentally, it was observed that the separation of the cylindrical lenses was one of the key variables for achieving self-starting modelocking operation, which highlights that the systematic pump beam conditioning is key to optimising the Kerr-lens modelocking effect.

3 Performance characterisations

3.1 Temporal and spectral measurements

As described in detail in [8], self-starting modelocking was achieved at pump powers over 850 mW, and a maximum average output power of 116 mW was achieved at a pump power of 1.1 W. The repetition rate of the laser was measured using a fast silicon photodiode and the fundamental pulse repetition frequency was measured with an instrument-limited resolution of 15 kHz, as shown in Fig. 5a. To emphasise the long-term stability of the laser, the repetition rate was measured for a prolonged period, as shown in Fig. 5b, highlighting stable modelocked operation over more than an hour of unperturbed operation. The slope of the trace is due to the temperature change of the environment, and the 'jagged' features in the trace are due to the temperature control under the crystal, which utilised a Peltier cooling element and a basic thermostatic control circuit, causing a small periodic temperature variation of the crystal. Despite the imperfect temperature control of the system, the laser remained stably modelocked for more than 1 h in this example.

3.2 Dispersion optimisation

In previous work [8], we presented two-photon autocorrelation measurements showing 111 fs pulses produced at the modelocking average power of 116 mW with a 10 nm bandwidth centred at 794 nm. The duration of the pulses can be understood to originate from two sources: the first

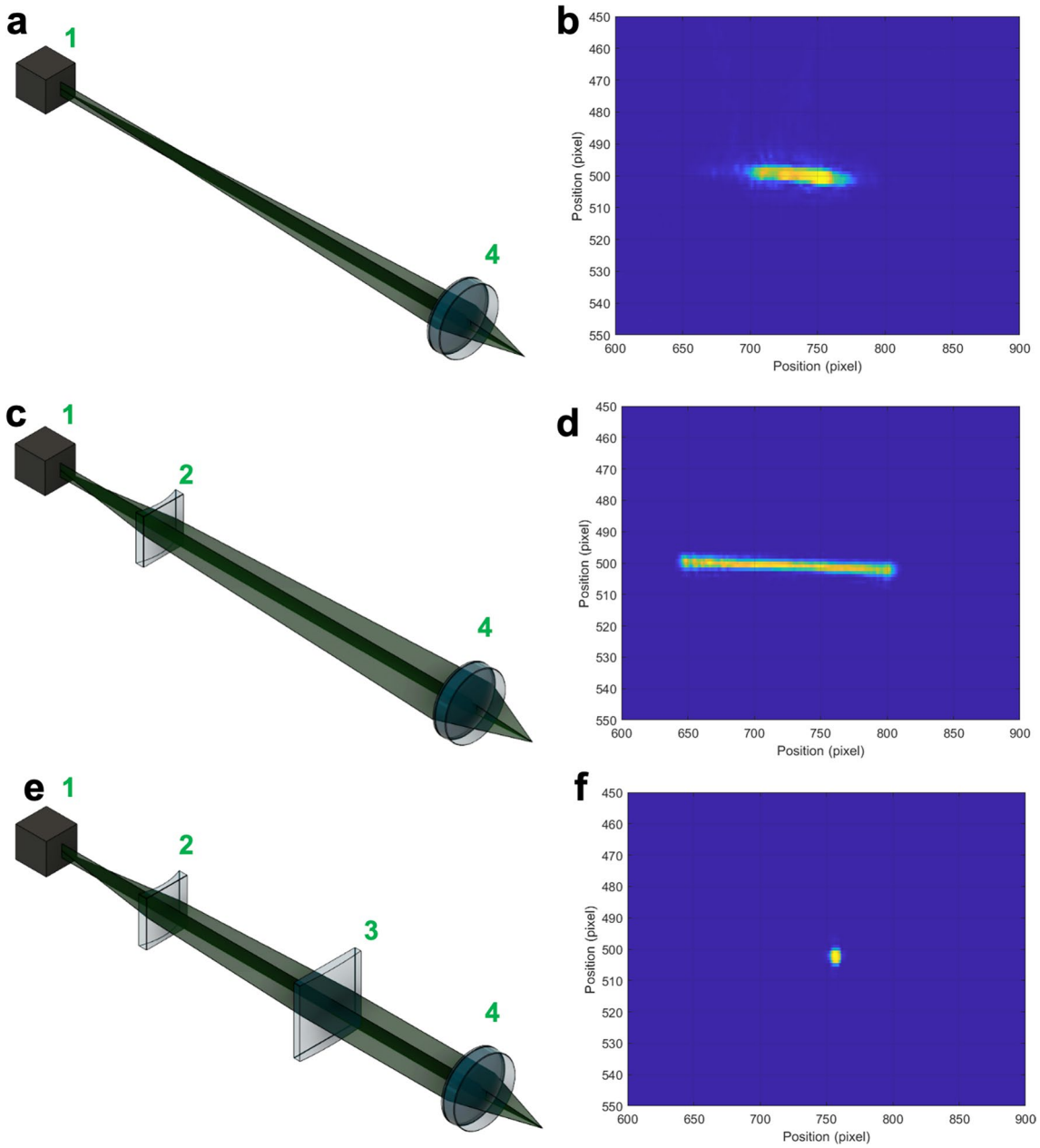

Fig. 4 **a**, **c** and **e** The step-by-step beam formatting of the diode beam. 1—laser diode with an integrated aspheric lens; 2—plano-concave cylindrical lens with f = -50 mm; 3—plano-convex cylindrical lens with f = + 300 mm, 4—achromatic doublet focussing lens with f = 35 mm; **b**, **d** and **f** corresponding images of the beam taken using a CCD camera after every step highlighting the change in beam propagation where one pixel corresponds to 2.9 µm × 3 µm

is due to chirp added by the out-coupling optics, since both the focussing lens and the separator (L_1 and M_S in Fig. 1a) add dispersion to the optical path of the pulse; and the second is due to the imperfect second-order group-delay dispersion (GDD) compensation in the laser cavity itself, which had excess negative GDD at the laser operating point. Here, we demonstrate sub-100-fs durations by better optimising the second-order intracavity dispersion.

The main element contributing to the dispersion inside the cavity is the crystal. To compensate the positive dispersion introduced by the optical cavity path inside the crystal, an off-the-shelf Gires–Tournois interferometer (GTI) plane mirror with a − 550 fs^2 GDD coating was included at the end of the cavity; however, this mirror did not provide perfect second-order group-delay dispersion (GDD) compensation, instead introducing excess negative GDD. Taking the GDD introduced by the crystal as + 60 fs^2 mm^{-1} [17] and the

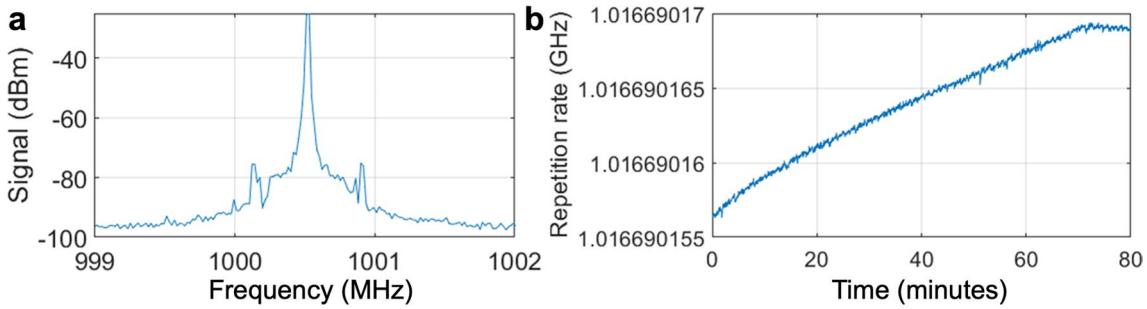

Fig. 5 **a** Detailed radio-frequency spectrum of the fundamental peak measurement recorded with a 15 kHz resolution bandwidth; **b** measurement of the fundamental repetition rate recorded over 1.2 h of operation

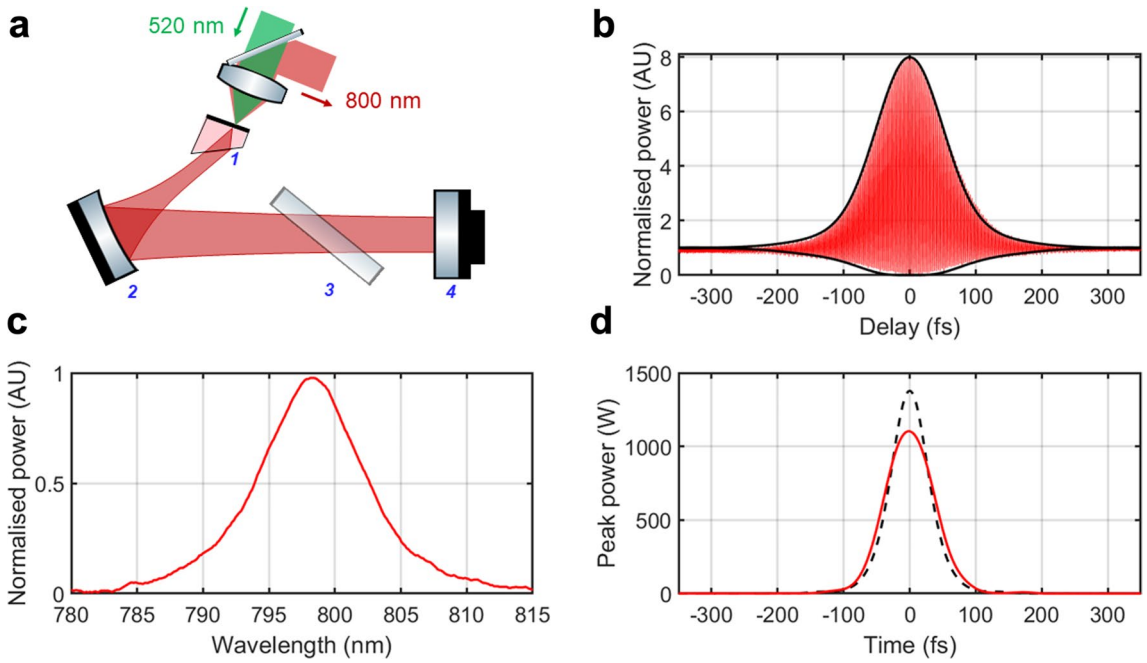

Fig. 6 **a** Cavity with a silica window introduced to compensate for second-order dispersion from the crystal and GTI mirror. 1—crystal; 2—curved mirror; 3—silica window; 4—GDD-coated end mirror. **b** TPA of the laser output with the silica window inside the cavity. **c** GDD-optimised modelocked spectrum. **d** GDD-optimised (red) and transform-limited (black dashed) modelled cavity pulse shapes

optical path of the crystal to be 3.5 mm (noting that the pulse propagates this path twice during one cavity roundtrip), the roundtrip intracavity GDD is found to be − 130 fs^2, which affects the length and shape of the pulses. This significant negative GDD affects the central wavelength of the modelocked spectrum, which shifts towards shorter wavelengths for shorter optical paths inside the crystal because of the GDD characteristics of the GTI mirror.

To demonstrate that improved intracavity dispersion management could yield shorter pulses, a 1 mm thick silica window was added into the cavity at Brewster's angle as shown in Fig. 6a and the cavity was realigned for modelocked operation. A separate set of measurements was recorded to evaluate the modelocked performance, which cannot be directly compared to the original cavity performance because the pulse characteristics were also sensitive to the exact cavity alignment. The average output power was found to reduce by 6% to 108 mW due to the additional loss. Assuming + 45 fs^2 mm^{-1} [17] dispersion added by the plate, the resulting intracavity GDD was estimated to be − 40 fs^2, which is much closer to optimal operation. A TPA of the resulting pulse can be seen in Fig. 6b, and the corresponding central wavelength of the modelocked spectrum was found to shift from 794 to 798 nm, with the FWHM being 9.5 nm. The new GDD-optimised trace with the additional chirp from the beam steering optics (red) and the estimated transform-limited pulse estimation (dashed black) are shown together in Fig. 6c, highlighting that the duration of the pulse has

reduced from 111 fs in the previous cavity design to 87 fs with the added Brewster-angled silica window, and the peak power has increased accordingly from 850 to 1100 W, which is closer to the predicted chirp-free pulse modelled in Fig. 6c.

4 Conclusions

In this paper, we have presented a detailed design and optimisation process for the construction of a self-starting Kerr-lens modelocked Ti:sapphire laser with a three-element cavity and a 1-GHz repetition rate, pumped by a single green diode laser. An ABCD computational model used for cavity design has been described in detail from basic principles and informs the laser configuration by predicting the intracavity mode sizes in both cw and modelocked operation. A systematic pump-beam formatting approach has been introduced, in which a 6:1 cylindrical-lens telescope is used to expand and collimate the slow axis of the pump beam, allowing optimal pump focussing in the crystal. In operation, the laser exhibited a self-starting modelocking threshold of 850 mW with a modelocked bandwidth of 9–10 nm and a central wavelength from 793 to 798 nm depending on the crystal insertion the cavity. The stability of the laser was demonstrated in free-running operation over more than an hour, with a clear repetition rate dependency on the environmental temperature highlighted. We have investigated the pulse duration changes on the dispersion management of the cavity and have shown that additional positive dispersion added to compensate for the off-the-shelf GTI coating of the end mirror has been effective in reducing the width of the pulses from 111 to 87 fs. Shorter pulses can be expected with an optimised compensation of the residual second- and third-order dispersion.

The laser design described utilises very few elements and is therefore compact enough to integrate within larger systems. The achieved peak powers of 870 W are expected to be sufficient for on-chip supercontinuum generation [18], and a GHz-range repetition rate with a wide spectral range makes the laser a promising candidate for precision astronomy applications [19]. The low-component design makes it compatible with a bonding method of oscillator building recently reported for a GHz-level Yb:ceramic system, which would allow the creation of a low-noise, ultra-robust turn-key laser system [20].

Author contributions H.O. and D.T. R. wrote the main manuscript, T.M. contributed to the results, P.C-M. contributed to early experimental configurations, all authors reviewed the manuscript.

Funding This study was supported by Science and Technology Facilities Council, ST/V000403/1, ST/T000635/1, ST/V000403/1, Engineering and Physical Sciences Research Council, EP/P005446/1.

Data availability Data underlying the results presented in this paper are not publicly available at this time but may be obtained from the authors upon reasonable request.

Declarations

Competing interests The authors declare no competing interests.

References

1. P.W. Roth, A.J. Maclean, D. Burns, A.J. Kemp, Opt. Lett. **34**, 3334 (2009)
2. P.W. Roth, A.J. Maclean, D. Burns, A.J. Kemp, Opt. Lett. **36**, 304 (2011)
3. M. Murayama, Y. Nakayama, K. Yamazaki, Y. Hoshina, H. Watanabe, N. Fuutagawa, H. Kawanishi, T. Uemura, H. Narui, Phys. Status Solidi A **215**, 1700513 (2017)
4. A. Michiue, T. Miyoshi, T. Kozaki, T. Yanamoto, S. Nagahama, and T. Mukai, IEICE Trans. Electron. **E92-C**, 194 (2009).
5. S. Backus, M. Kirchner, C. Durfee, M. Murnane, H. Kapteyn, Opt. Express **25**, 12469 (2017)
6. K. Gürel, V.J. Wittwer, M. Hoffmann, C.J. Saraceno, S. Hakobyan, B. Resan, A. Rohrbacher, K. Weingarten, S. Schilt, T. Südmeyer, Opt. Express **23**, 30043 (2015)
7. P. Castro-Marin, T. Mitchell, J. Sun, D.T. Reid, Opt. Lett. **44**, 5270 (2019)
8. H. Ostapenko, T. Mitchell, P. Castro-Marin, D.T. Reid, Opt. Express **30**, 39624 (2022)
9. H. Kogelnik, T. Li, Appl. Opt. **5**, 1550 (1966)
10. H. Kogelnik, E. Ippen, A. Dienes, C. Shank, IEEE J. Quantum Electron. **8**, 373 (1972)
11. B.E. Bouma, J.G. Fujimoto, Opt. Lett. **21**, 134 (1996)
12. M. Paye, Massachusetts Institute of Technology (1994)
13. M. Sheik-Bahae, A.A. Said, D.J. Hagan, M.J. Soileau, W.W. Van Stryland, Opt. Eng. **30**, 1228 (1991)
14. B.E. Bouma, M. Ramaswamy-Paye, J.G. Fujimoto, Appl. Phys. B: Lasers Opt. **65**, 213 (1997)
15. V. Magni, G. Cerullo, S. De Silvestri, Opt. Commun. **101**, 365 (1993)
16. H.A. Haus, J.G. Fujimoto, E.P. Ippen, IEEE J. Quantum Electron. **28**, 2086 (1992)
17. M.N. Polyanskiy, Available from: https://refractiveindex.info (2022).
18. H. Zhao, B. Kuyken, S. Clemmen, F. Leo, A. Subramanian, A. Dhakal, P. Helin, S. Severi, E. Brainis, G. Roelkens, R. Baets, Opt. Lett. **40**, 2177 (2015)
19. T. Steinmetz, T. Wilken, C. Araujo-Hauck, R. Holzwarth, T.W. Hänsch, T. Udem, Appl. Phys. B **96**, 251 (2009)
20. Y. Feng, T.P. Lamour, H. Ostapenko, R.A. McCracken, O. Mandel, D. Weise, D.T. Reid, Opt. Lett. **46**, 5429 (2021)